Effect of Curvature Radius on Single Droplet Dynamic Characteristic within Concave-Wall Jet

Bin Gong , Aibo Jian , Jing Zhang * , Guang Yang , Yifeng Liu

Posted Date: 18 December 2023

doi: 10.20944/preprints202312.1261.v1

Keywords: concave-wall jet; droplet; heterogeneous; interfacial energy; deformation mechanism

Article

Effect of Curvature Radius on Single Droplet Dynamic Characteristic within Concave-Wall Jet

Bin Gong [1], Aibo Jian [1], Jing Zhang [1,2,*], Guang Yang [1] and Yifeng Liu [1]

[1] School of Mechanical and Power Engineering, Shenyang University of Chemical Technology, Shenyang 110142, China; gbsyhgdx@163.com (B.G.); jab15840350353@163.com (A.J.); 1044604212@qq.com (G.Y.); 1614677150@qq.com (Y.L.)

[2] School of Chemical Engineering & Technology, Tianjin University, Tianjin 300350, China

* Correspondence: 2501474185@qq.com; +86-13478887170.

Abstract: The centrifugal force field in the hydrocyclone was affected by the concave-wall curvature radius R_0, the mechanism of droplet deformation was closely related to the mass transfer efficiency. Numerical simulation and experimental data were collected to reveal the deformation characteristics and mechanism of single droplet crossing concave-wall jet. Normalized interfacial energy γ and stretching performance were provided to investigate the droplet deformation process. The results showed that the droplet was stretched along the streamwise and shrank along the spanwise in the concave-wall jet. The droplet interfacial energy and deformation were the largest when the droplet crossed the jet boundary at t = 0.20 s. Maximum γ value increased with the increase of R_0 by 57.3% to 71.4%, and the distance between droplet and concave-wall increased with R_0. Q-criterion was exported to show the vortex strength increasing as the decrease of R_0 in the jet boundary. The pressure distribution inside the droplet showed that the pressure decreased as R_0 increased, while the pressure difference increased along the streamwise and wall-normal direction. The study suggested that the droplet breakup was more difficult for the smaller R_0, which was beneficial for liquid-liquid heterogeneous separation.

Keywords: concave-wall jet; droplet; heterogeneous; interfacial energy; deformation mechanism

1. Introduction

Liquid-liquid heterogeneous flow process was widely applied in the chemical industry [1]. An in-depth analysis of droplet deformation and breakup contributed to the design and optimization of dispersed multiphase flows [2]. The disruptive shear stress can be found at the jet boundary vortices. The droplet deformation or breakup was caused by the shear stress, and the mass transfer between the phases was determined by droplet surface area [3–5]. To predict and evaluate the separation or mixing processes of multiphase flow, the droplet deformation mechanism was investigated for exploring the mass transfer processes, such as liquid-liquid heterogeneous phase mixing and separation.

When a droplet traversed a vortex, the uneven energy was transferred to the droplet surface from the vortex, which resulted in the deformation or breakup of droplet. Andersson developed an energy criterion to predict droplet breakup, which occurred when the turbulent kinetic energy of vortex attained a critical value. The energy-critical value was calculated by the interfacial energy of mother drop and the breakup criterion was defined as the interfacial energy increase for drop deformed complex [6]. Andersson revealed that the deformed drops attained the maximum value of interfacial energy before breakup, and more energy was required to be transferred from the turbulent vortices for breakup [7,8]. The drop breakup in the turbulent flow was mainly caused by the turbulent pressure fluctuation mechanism when the Ohnesorge number was less than 0.01. Chen et al. proposed that the drop breakup criteria depended on the degree of surface deformation prior to breakup, and the relationship between turbulent eddies and drop breakup was established and quantified [9]. Han et al. proposed a theoretical model based on the theories of isotropic turbulence that the drop breakup was based on interfacial energy density increase [10]. As mentioned above, the

 doi:10.20944/preprints202312.1261.v1

interfacial energy played a key role in the study of droplet deformation and breakup. The reason for drop breakup was that droplets were subject to large-scale deformations prior to breakup, and the surface oscillation was obvious.

Experimental study of the droplet deformation mechanism was difficult and the deformation process can only be studied by monitoring the drop behavior. However, Computational fluid dynamics (CFD) simulation offered a solution to overcome these obstacles. The drop dynamic characteristic in multiphase flow systems was investigated by large eddy simulation (LES) [11–14], and volume of fluid (VOF) method was usually used to obtain the interface deformation due to the complexity of interface topology [15,16]. A combination of LES and VOF was used to research the interaction between jet and drop and predicted the complex interface of deformed droplets [17–21]. To prevent numerical diffusion of density and viscosity at the drop interface, the Geo-Reconstruct scheme was used to reconstruct the grid during computation. Additionally, the dynamic adaptation meshing technique was applied to manage mesh encryption at the liquid-liquid heterogeneous interface [22–25]. The above numerical simulation approach has been recognized as a classic reference to study the droplet dynamic characteristic, as studied by Charin [26]. Although Charin's study focused on the rising droplet, the behavior of single droplet dynamics in the continuous-phase was similar. The dynamic adaptation mesh refinement technique promoted the study of LES-VOF numerical simulation in droplet deformation and breakup.

Our previous research found that the wall jet flow was affected by the curvature radius of concave-wall in two ways, the jet spread in radial direction shrank [27] and the instability at the jet boundary increased [28]. Within the possible studies in concave-wall jet, the intrinsic and extrinsic factors of droplet deformation were the particular interest to this paper. The LES-VOF model was used to study the deformation mechanism of carbon tetrachloride (CCl_4) droplet in the concave-wall jet with water as the continuous-phase. The droplet dynamic characteristic was investigated based on the centrifugal force field which was created by the concave-wall jet with various curvature radii.

2. Numerical Simulation

2.1. Physical Models and Materials

Figure 1a depicts the falling process of a CCl_4 droplet in a vertical cylinder filled with water. The jet inlet section was made into a semicircular shape with a radius of 15 mm (R = 15 mm), where θ = 0° was the circumferential coordinate of jet inlet. Since the study focused on the localized flow near the concave-wall at the jet inlet, the annular channel at -15° < θ < 35° was retained as the study domain considering the jet inlet entraining effect, which is depicted in Figure 1b. The coordinate system in Figure 1b was converted from the cylindrical coordinate system in Figure 1a with the following conversion equation:

$$l = \frac{\theta}{180}\pi R_0 \tag{1}$$

$$n = R_0 - r \tag{2}$$

Where l is the streamwise coordinate, n is the wall-normal coordinate, and R_0 is the curvature radius of concave-wall.

Preprints (www.preprints.org) | NOT PEER-REVIEWED | Posted: 18 December 2023 doi:10.20944/preprints202312.1261.v1

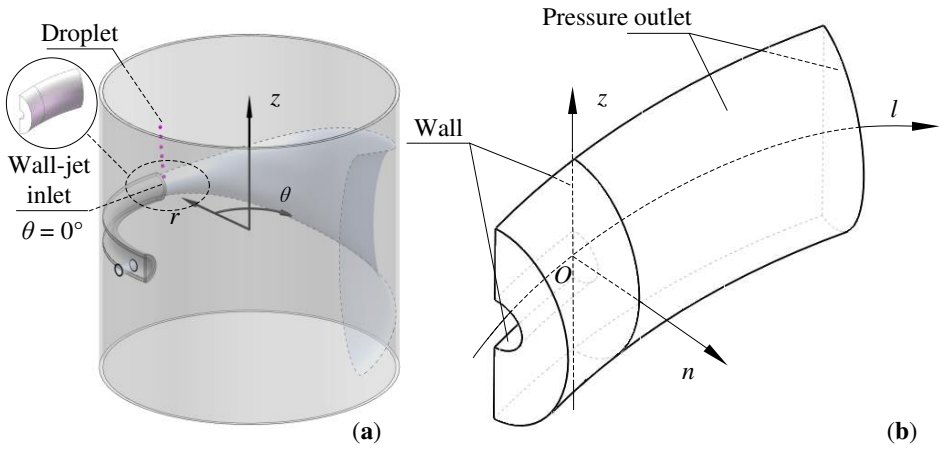

Figure 1. (**a**) Physical model of the droplet falling process in the vertical cylinder with a semicircular shape inlet; and (**b**) computational domain and boundary conditions.

2.2. Numerical Simulation Method and Boundary Conditions

The numerical framework was implemented in Ansys Fluent 16.2, the unsteady turbulent flow was computed by three-dimensional double-precision implicit solver. LES and VOF models were coupled to explore the fluid dynamics of CCl_4 drop deformation in the concave-wall jet under purified water conditions. Physical properties of the binary system are described in Table 1. The VOF model relied on the discrete-phase volume fraction α, the cell was situated at the heterogeneous interface when $0 < \alpha < 1$, indicating that the volume fraction of CCl_4 was α, and that of water was 1-α. The body forces were treated refer to the continuum surface force model [29].

PISO algorithm was used to deal with pressure-velocity coupling and PRESTO! scheme was applied for the pressure discretization in large eddy simulation. The momentum equation was discretized by the Bounded Central Differencing scheme. Geo-reconstruct scheme was utilized to track the phase interface in the computing cell. The dynamic adaptive approach was employed to refine the droplet boundary mesh.

Table 1. Physical parameters of continuous-phase (Water) and discrete-phase (CCl_4) at T = 293.15 K.

Continuous-phase	Value	Discrete-phase	Value
Density ρ/kg·m^{-3}	998.2	Density ρ_p/kg·m^{-3}	1595.0
Viscosity/m^2·s^{-1}	1.003×10^{-6}	Viscosity/m^2·s^{-1}	9.69×10^{-4}
Jet inlet velocity u_{in}/m·s^{-1}	0.55	Droplet diameter d_p/mm	5.6
Interfacial tension σ/mN·m^{-1}		45.7	
Gravity g/m·s^{-2}		-9.81	

The boundary conditions were as follows: Jet inlet was set as velocity-inlet (u_{in}), while the outlet was defined as pressure-outlet with a gauge pressure of 0. The solid wall was smooth and non-slip. A gravitational field with a magnitude of -9.81 m·s^{-2} in the Z-direction was applied. In terms of the discrete-phase initialization, the CCl_4 droplet was defined as a sphere for falling into the jet. The droplet center was arranged at z = 40 mm, n = 5 mm and l = 10 mm from jet inlet. The time-step size was set as 10 μs unsteady calculation and 200 computing steps was the maximum value to ensure convergence limited to 10^{-5} in each time-step.

2.3. Mesh Division and Independence Analysis

To obtain a three-dimensional hexahedral grid, the computational domain was divided into two parts bounded by the jet inlet section. The flow domain in the study was meshed by ICEM software with refinement near the concave-wall, as illustrated in Figure 2. The mesh independence analysis

 doi:10.20944/preprints202312.1261.v1

was performed in two steps: (i) the various grid densities were employed for the same computational domains (Grid-1, Grid-2, Grid-3), and (ii) the various computational domain sizes were used for the same grid density condition (Grid-2, Grid-4, Grid-5). Due to the flow characteristic of concave-wall jet, the droplet dynamics were greatly impacted by the spanwise size of computational domain, and the effect of wall-normal size was smaller. Therefore, the spanwise sizes of Grid-2, Grid-4, and Grid-5 were adjusted to 120 mm, 80 mm, and 200 mm respectively, while the wall-normal sizes remained the same.

The five grid schemes were applied to the case of a drop with d_p = 5.6 mm, u_{in} = 0.55 m·s^{-1}, and R_0 = 300 mm where the droplet surface area (A_p) was obtained from multi-time computational results. Maximum values of A_p were compared at the period of t = 0.00 ~ 0.30 s, and the specific simulation results were presented in Table 2. The simulation data indicates that the droplet maximum surface areas of Grid-2, Grid-3 and Grid-5 were similar when the identical computational settings were assessed. The A_p deviation of Grid-2 and Grid-3 was only 5.1%, while that of Grid-2 and Grid-5 was 4.7%. Considering the accuracy of simulated data, the computational domain setting and meshing scheme of Grid-2 were selected to save computational time and storage space. The total number of meshes ranged from 1005855-1061886 for different structure models, and the mesh size near the concave-wall was 0.05 mm.

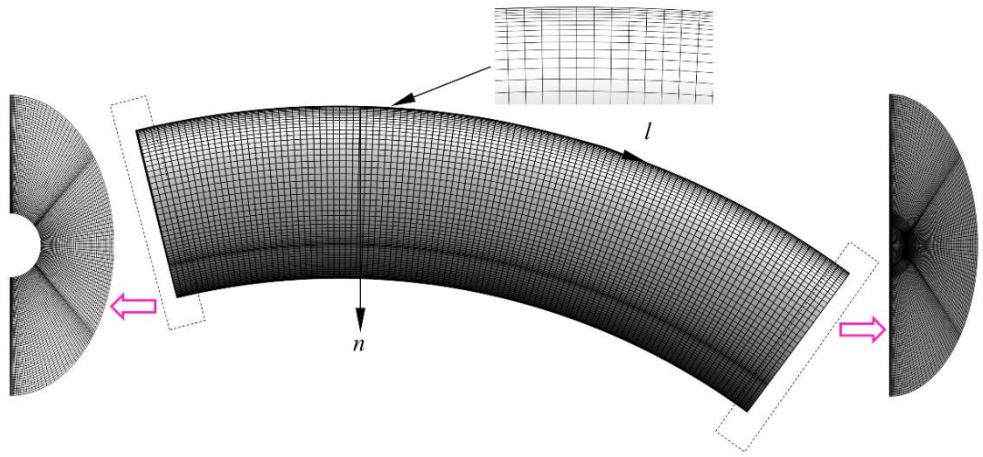

Figure 2. Three-dimensional hexahedral mesh employed for simulations.

Table 2. Mesh independence test performed for the case of d_p = 5.6 mm, u_{in} = 0.55 m·s^{-1} and R_0 = 300 mm.

	Number of grids	Computational domain volume/mm^3	Maximum of A_p /mm^2
Grid-1	529142	633083	141.27
Grid-2	1034352	633083	166.65
Grid-3	1539646	633083	168.92
Grid-4	994088	359522	176.21
Grid-5	1492080	2596751	163.28

2.4. Experimental validation

Our team provided an experimental system utilized to capture images of the dynamic process of droplet deformation and breakup in a concave-wall tangential jet [30]. Figure 3 illustrated the experimental setup which was consisted with three components: water jet system, CCl_4 droplets generator and real-time image acquisition system. A lighting device was installed opposite to the camera to obtain clear images (see Figure 3). The numerical simulations performed in this paper were validated by data in which five droplets were obtained from the experiments, which proved the precision of simulation scheme in foretelling the process of droplet deformation and breakup. Figure

Preprints (www.preprints.org) | NOT PEER-REVIEWED | Posted: 18 December 2023 doi:10.20944/preprints202312.1261.v1

4 offers a comparison of the drop centroid position between the experimental data and simulation data using the LES-VOF method. The simulation result demonstrated similar trends to the experimental data concerning the relative positions of the drop centroid position and the jet inlet. All simulated data existed within the experimental data range, indicating the possibility of using the numerical simulation scheme to describe the dynamic behavior of droplet passing through the concave-wall jet.

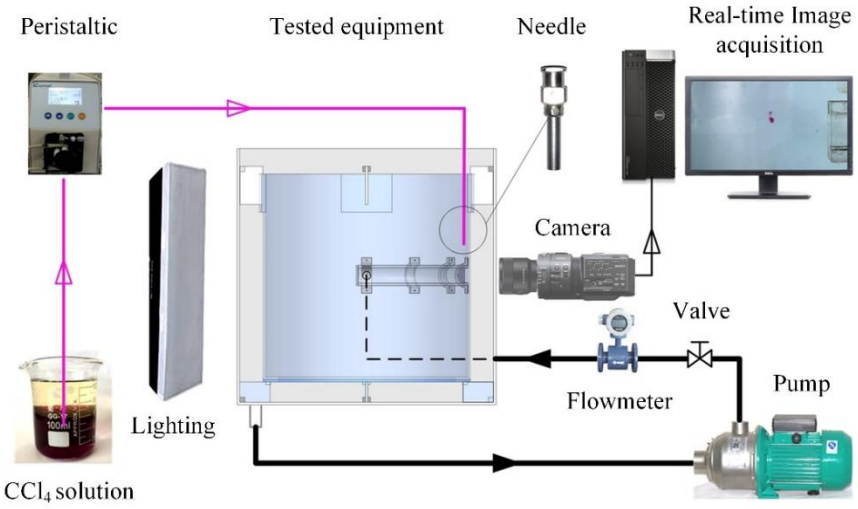

Figure 3. Experimental setup for single droplet in concave-wall jet. (**1**) cylinder; (**2**) circulating water inlet; (**3**) semi-circular annulus; (**4**) multiple holes plate; (**5**) concave-wall jet inlet; (**6**) needle support; (**7**) needle; (**8**) CCl_4 droplet; (**9**) concave-wall jet.

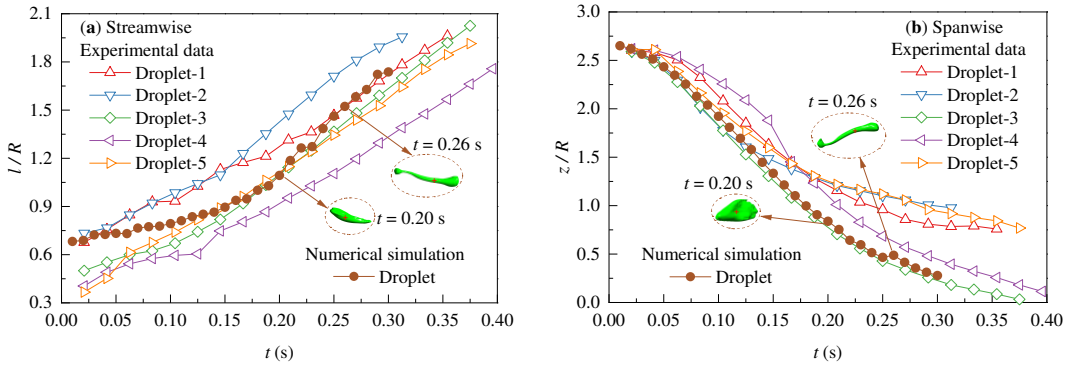

Figure 4. Comparison of experimental and simulation results of droplet centroid position along (**a**) the jet streamwise and (**b**) the jet spanwise (+ represented the droplet centroid position).

3. Results and analysis

With the decreasing of the concave-wall curvature radius R_0, the centrifugal force increased in the jet region and the jet expansion shrank along the wall-normal direction. The jet boundary flow was significantly influenced and droplet behaviors in the jet boundary were inevitably affected by R_0 for the heterogeneous phase flow.

3.1. Normalized Interfacial Energy

Studies showed that droplets interact with vortices in the flow field and the phase-interface contact area of droplet increased by consuming vortex energy [31]. In the concave-wall jet, the droplet was mainly stretched along the streamwise, and the heterogeneous interface area and interfacial energy increased. The interfacial energy was defined as the product of the interfacial tension

Preprints (www.preprints.org) | NOT PEER-REVIEWED | Posted: 18 December 2023 doi:10.20944/preprints202312.1261.v1

coefficient and the instantaneous interfacial area. The normalized interfacial energy γ was a dimensionless parameter of droplet deformation.

$$\gamma(t) = \frac{\sigma A_{\mathrm{p}}}{\sigma A_{\mathrm{p0}}} = \frac{A_{\mathrm{p}}}{A_{\mathrm{p0}}} \tag{3}$$

Where A_{p0} is the droplet area at the initial time t = 0 s, the droplet was spherical, and γ = 1.

To investigate the effects of the concave-wall curvature radius on droplet deformation and breakup, the normalized interfacial energy of droplet was analyzed as shown in Figure 5. It is seen that the droplet fell outside of the jet at $t \le 0.16$ s, the interfacial area of droplet was decreased as R_0 increased. At t = 0.16 s, the γ-value of R_0 = 400 mm decreased by 8.4% compared to that of R_0 = 150 mm. The interfacial area increased rapidly at t = 0.16 ~ 0.25 s, and the breakup occurred at $t \approx 0.26$ s. The maximum increment of the interfacial energy was 53.7% (R_0 = 200 mm) ~ 71.4% (R_0 = 400 mm), which translated to $\gamma_{\max}$ = 1.54 ~ 1.71. These agreed with the experimental estimate $1.26 < \gamma < 1.92$ for droplet deformation before breakup [8]. After $t > 0.26$ s, the mother droplet broke into daughter droplets, causing the total interfacial area to significantly decrease due to the shrinkage of the daughter droplets into an approximate ellipsoidal shape after breakage.

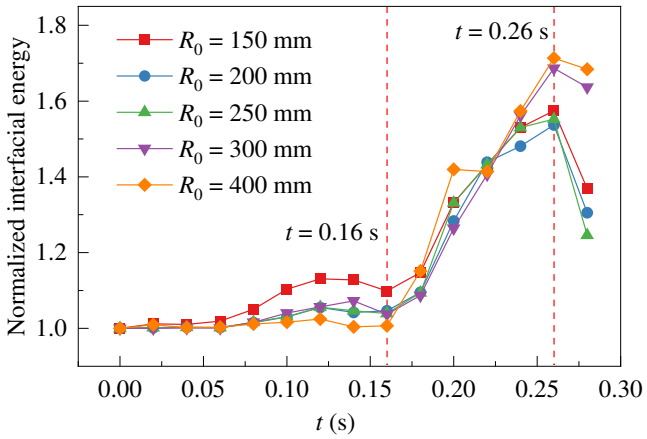

Figure 5. Effect of concave-wall curvature radii on normalized interfacial energy of droplets.

3.2. Deformation Properties

Both shear stress and normal stress were the keys to the droplet breakup in turbulent flow [8]. When a droplet enters the jet boundary, the shear rate around the drop significantly changes. The concave-wall curvature radius played a crucial role in the distribution of shear stress and centrifugal force at the jet boundary, directly affecting on the droplet dynamic behaviors. To gain insight into the droplet deformation properties as affected by the centrifugal force field, we analyzed of the droplet deformation dimensions along the streamwise L_{l} and wall-normal direction L_{n}. Figure 6 shows the dimensionless size analysis based on the droplet's initial diameter d_{p}.

It can be seen that the droplet stretching processes were similar in different centrifugal force fields based on R_0. Figure 6a shows the droplet deformation along the streamwise, and the deformation rate was accelerated when the droplet entered the jet region after t = 0.16 s. At t = 0.20 ~ 0.26 s, L_{l} of droplet was longer with the increasing R_0. In Figure 6b, droplets were stretched $L_{\mathrm{n}}/d_{\mathrm{p}}$ = 0.9 ~ 1.2 at $t \le 0.16$ s. At t = 0.16 ~ 0.20 s, the droplet entered the jet boundary, the droplet size was close to $L_{\mathrm{n}}/d_{\mathrm{p}} \approx 1.0$. At $t \ge 0.20$ s, while the droplet was in the concave-wall jet, the droplet rapidly shrank along the wall-normal direction under the centrifugal force.

Preprints (www.preprints.org) | NOT PEER-REVIEWED | Posted: 18 December 2023 doi:10.20944/preprints202312.1261.v1

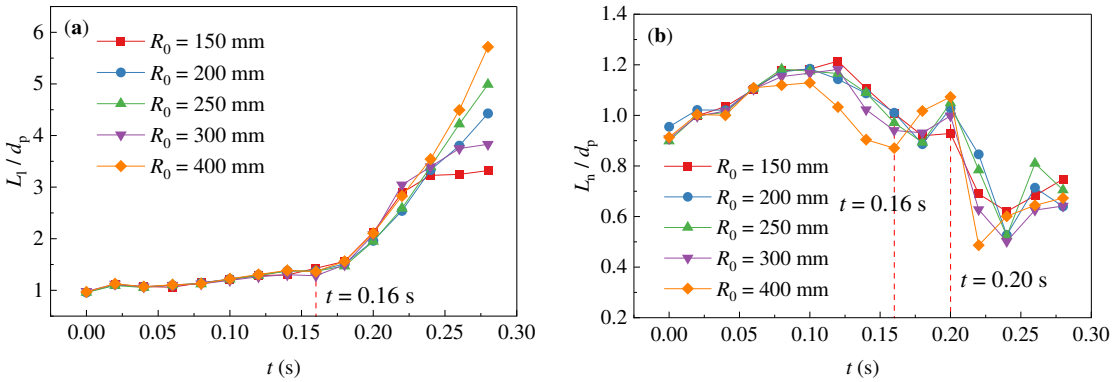

Figure 6. Dimensionless size of droplet along (**a**) the streamwise and (**b**) wall-normal direction.

From Figure 5 and Figure 6, the results were summarized in that the droplet deformation process was divided into three stages. Outside the jet, the droplets were only subjected to the flow resistance of continuous-phase, and the spreading deformation occurred along the streamwise and wall-normal direction ($L_n < L_l$). Within the jet boundary, the shear rate in the streamwise was much greater than the wall-normal direction, and the droplets were stretched along the streamwise, while $L_n \approx d_p$. In the core area of potential flow, the centrifugal force field caused the droplets to approach the concave-wall, and the droplets contracted along the wall-normal direction by the wall restricted. When $L_n << L_l$, the drop broke up into multiple daughter droplets. Therefore, this study focused on the droplet in the jet boundary at t = 0.20 s and investigated the influence of the concave-wall curvature on the droplet deformation mechanism.

3.3. Q-criterion Based Vortex Analysis of a Concave-wall Jet

The Q-criterion was a well-established method for identifying vortices. Constantinescu et al. suggested that the second invariant of the velocity gradient tensor was defined as the quantity Q, vortices can be pointed when $Q > 0$ [32]. To understand the droplet deformation process in the concave-wall jet, the Q-criterion was used to accurately locate the core of vortices. Figure 7 shows the flow field at the critical moment (t = 0.20 s) when the droplet entered the jet boundary. Within this study, a Q threshold of 53 s^{-2} (Level = 0.01) was selected to describe vortices, vortices with varying sizes can be found in the concave-wall jet boundary. The droplet was visualized using the isosurface of volume fraction of CCl_4 α = 0.5 and colored black to indicate its location and shape.

According to the Q-criterion, we can observe the vortices generated at the jet boundary. It can be seen that the continuous-phase flow field was influenced by the concave-wall curvature radius. With an increased R_0, the region of $Q > 53$ s^{-2} reduced, the distance between neighboring vortices grew larger, and the influence range of vortices became narrower along the spanwise. The dimensionless velocity parameter u/u_{in} revealed that the $u/u_{in} > 0.5$ regions shrank both streamwise and spanwise, and the continuous-phase velocity in vortices decreased. This also indicated that the vortex strength decreased as the concave-wall curvature radius increased.

At t = 0.20 s, the droplet exhibited a unique "high left and low right" shape and a part of the droplet far from the jet inlet entered the jet boundary region. The droplet swiftly spread out and formed a thin sheet that integrated closely to the jet boundary region, it underwent the spreading deformation process along the streamwise in the jet boundary. As R_0 increased, the stretching length along the streamwise grew due to the decrease in centrifugal force, while the sheet thickness along the spanwise remained unchanged. Interestingly, the droplet fell and triggered the formation of vortices in the surrounding fluid, and the strength of these vortices around the droplet grew in proportion to R_0, as indicated by the increasing u/u_{in} value.

Preprints (www.preprints.org) | NOT PEER-REVIEWED | Posted: 18 December 2023 doi:10.20944/preprints202312.1261.v1

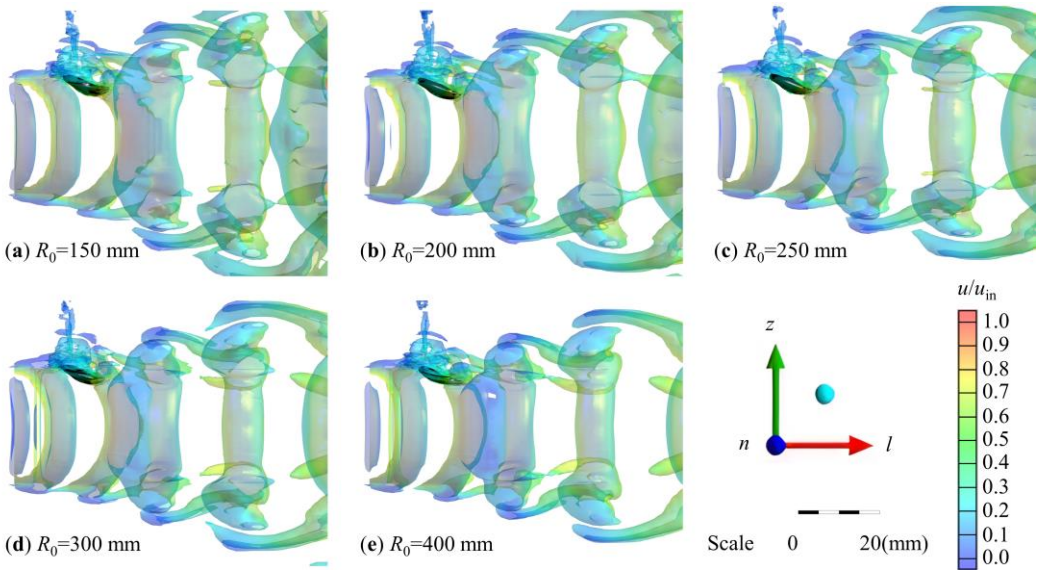

Figure 7. Droplet deformation and interaction with jet boundary vortices at t = 0.20 s based on different concave-wall curvature radii. (**a**) R_0 = 150 mm; (**b**) R_0 = 200 mm; (**c**) R_0 = 250 mm; (**d**) R_0 = 300 mm; (**e**) R_0 = 400 mm. The droplet was colored black and vortices were colored by velocity magnitude.

3.4. Pressure Field Distribution Inside the Droplet

Droplet deformation was a form of energy transfer, and Wang and his team discovered that there was a direct correlation between the additional hydrostatic energy consumption and the droplet stretching and deformation [32]. The pressure distribution of multiple sections along the spanwise was applied for studying the droplet internal pressure at t = 0.20 s, as shown in Figure 8. The droplet exhibited that a region (left side of the droplet) with positive pressure was outside the jet and a region (right side of the droplet) with negative pressure was in the jet boundary. Figure 8 shows that the volume of negative pressure region inside the droplet increased significantly with the increase in R_0. The reason is that the jet width narrowed along the wall-normal direction because the centrifugal force was strengthened when the R_0 value was smaller. The streamwise size of the droplet was elongated with an increase of R_0, L_1 of R_0 = 400 mm rises by 10.1% than L_1 of R_0 = 150 mm. Therefore, the droplet was easily broken for the larger R_0 value.

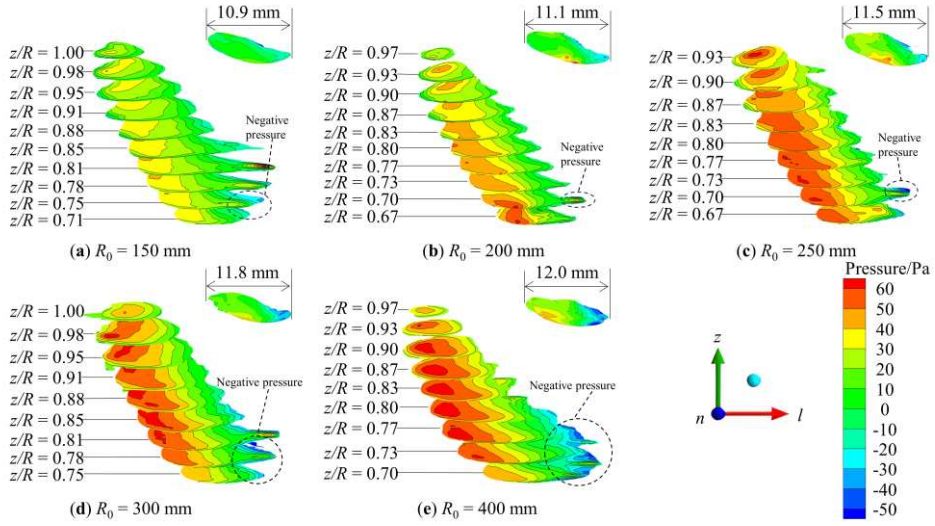

Figure 8. Effect of the concave-wall curvature radius on pressure distribution inside the droplet at t = 0.20 s. (**a**) R_0 = 150 mm; (**b**) R_0 = 200 mm; (**c**) R_0 = 250 mm; (**d**) R_0 = 300 mm; (**e**) R_0 = 400 mm. The spacing within the figure has been stretched along the spanwise for clarity.

Preprints (www.preprints.org) | NOT PEER-REVIEWED | Posted: 18 December 2023 doi:10.20944/preprints202312.1261.v1

In Figure 9, the pressure distribution inside the droplet was analyzed along the streamwise and wall-normal direction. As shown in Figure 9a, the pressure distribution followed a similar trend, with the highest pressure of 50 Pa occurring at l = 15 mm. The droplet pressure near the jet inlet was lower, and the pressure increased with R_0. A negative pressure region existed inside the droplet away from the jet inlet, but there was no negative pressure inside the droplet for R_0 = 150 mm. As the curvature radius increased, the region and value of negative pressure all increased. This indicates that the pressure difference inside the droplet increased, increasing the droplet length along the streamwise. Figure 9b reveals that the near-wall pressure of droplet formed significant peaks when R_0 = 150 mm, R_0 = 200 mm, and R_0 = 250 mm. When R_0 = 300 mm, the droplet pressure remained essentially constant, while the pressure of R_0 = 400 mm displayed a linear increase along the wall-normal direction. It was found that the pressure difference near the concave-wall in the droplet decreased as the curvature radius decreased. However, the total pressure difference in the drop was lower for R_0 = 150 mm and R_0 = 200 mm. The droplet distance from the wall increased with the reducing R_0 although the centrifugal force field was enhanced near the concave-wall. For the smaller R_0 value, it was difficult for the droplet to break because the pressure difference inside the droplet was smaller and the distance from the wall increased.

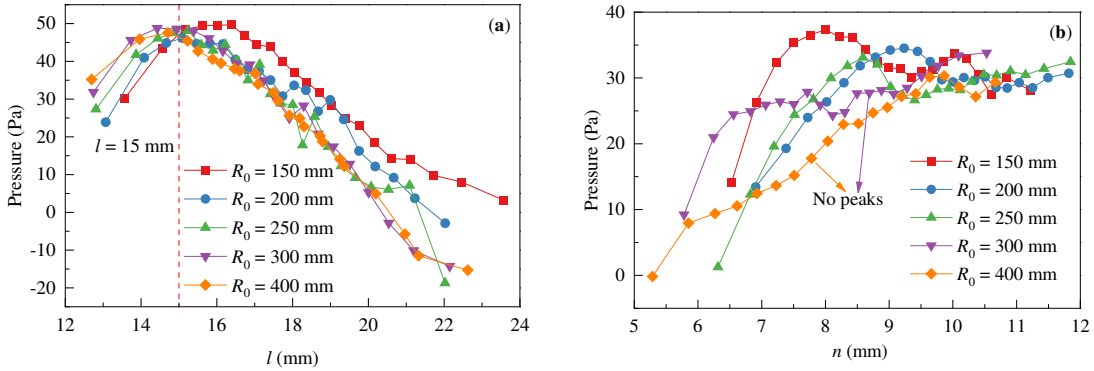

Figure 9. Distribution of pressure inside the droplet along (**a**) the streamwise and (**b**) the wall-normal direction (t = 0.20 s).

4. Conclusions

The LES-VOF model was employed to perform numerical simulations on the process of single droplet into the concave-wall jet. Three stages of droplet behaviors were obtained, including free-falling outside the jet, spreading at the jet boundary, and ultimately leading to a breakup. In this study, the effect of concave-wall curvature radius on dynamic characteristics of droplet received special attention at the jet boundary.

The investigation revealed that the normalization interfacial energy significant growth during the droplet crossed the jet boundary, and maximum interfacial energy (γ_{max}) ranged from 1.54 to 1.71. Further analysis of the Q-criterion revealed the structure of multi-vortices at the jet boundary, which led to the droplet spreading deformation. The stretched size along the streamwise (L_1) and γ_{max} all increased with R_0, therefore, reducing the R_0 could effectively decrease droplet spreading deformation and interfacial energy. The study suggested that the intensity and influence range of vortices decreased with the increase of R_0, while the droplet breakup was more difficult for the smaller R_0 although the centrifugal force was enhanced near the concave-wall. Some results of the droplet were presented that the streamwise size was smaller, the total pressure difference in the drop was lower, and the droplet distance from the wall was larger when R_0 was provided as a smaller value. The study provided the theoretical basis for the structural design of the concave-wall jet in liquid-liquid heterogeneous phase separation equipment.

Author Contributions: Methodology, Writing-Original draft preparation, B.G.; Software, Validation, Software Data curation, A.J.; Writing- Reviewing and Editing, J.Z.; Supervision, G.Y.; Visualization, Investigation, Y.L. All authors have read and agreed to the published version of the manuscript.

Funding: This research was funded by the Applied Basic Research Program Project of Liaoning Province of China, grant number 2022JH2/101300077 and the Basic Research Projects of Higher Education Institutions of Education Department of Liaoning Provincial of China, grant number JYTMS20231507.

Data Availability Statement: The data presented in this study are available on request from the corresponding author.

Conflicts of Interest: The authors declare no conflict of interest.

References

1. Zhang, M. y.; Liu, X. z.; Zhang, C. c.; Li, X. y.; Zhang, H.; Tan, Z. w.; Zhang, L. h.; Wang, Z. b., Numerical investigation of shear flow structure induced by guided vane in a liquid-liquid cyclone reactor. *Chem. Eng. Process.* **2021,** 167, 108521.
2. Fu, Y. h.; Wang, H.; Zhang, X.; Bai, L.; Jin, Y.; Cheng, Y., Numerical simulation of liquid mixing inside soft droplets with periodic deformation by a lattice Boltzmann method. *J Taiwan Inst Chem Eng* **2019,** 98, 37-44.
3. Liu, H. h.; Lu, Y.; Li, S.; Yu, Y.; Sahu, K. C., Deformation and breakup of a compound droplet in three-dimensional oscillatory shear flow. *Int. J. Multiphase Flow* **2021,** 134, 103472.
4. Foronda-Trillo, F. J.; Rodríguez-Rodríguez, J.; Gutiérrez-Montes, C.; Martínez-Bazán, C., Deformation and breakup of bubbles interacting with single vortex rings. *Int. J. Multiphase Flow* **2021,** 142, 103734.
5. Xu, Z. k.; Wang, T. y.; Che, Z. z., Droplet breakup in airflow with strong shear effect. *J. Fluid Mech.* **2023,** 941, A54.
6. Andersson, R.; Andersson, B., Modeling the breakup of fluid particles in turbulent flows. *AlChE J.* **2006,** 52, (6), 2031-2038.
7. Andersson, R.; Helmi, A., Computational fluid dynamics simulation of fluid particle fragmentation in turbulent flows. *Appl. Math. Model.* **2014,** 38, (17-18), 4186-4196.
8. Andersson, R.; Andersson, B., On the breakup of fluid particles in turbulent flows. *AlChE J.* **2006,** 52, (6), 2020-2030.
9. Chen, Y. j.; Ding, J.; Weng, P. f.; Yang, X. q.; Wu, W. j., On the breakup of Taylor length scale size bubbles and droplets in turbulent dispersions. *Chem. Eng. J.* **2020,** 386, 121826.
10. Han, L.; Luo, H. a.; Liu, Y., A theoretical model for droplet breakup in turbulent dispersions. *Chem. Eng. Sci.* **2011,** 66, (4), 766-776.
11. Karthik, G. M.; Thaker, A. H.; Buwa, V. V., Particle-resolved simulations of catalytic fixed bed reactors: Comparison of turbulence models, LES and PIV measurements. *Powder Technol.* **2020,** 361, 474-489.
12. Gomez-Flores, A.; Heyes, G. W.; Ilyas, S.; Kim, H., Effects of artificial impeller blade wear on bubble-particle interactions using CFD (k-ε and LES), PIV, and 3D printing. *Miner. Eng.* **2022,** 186, 107766.
13. Maniscalco, F.; Buffo, A.; Marchisio, D.; Vanni, M., Numerical simulation of bubble columns: LES turbulence model and interphase forces blending approach. *Chem. Eng. Res. Des.* **2021,** 173, 1-14.
14. Bao, Y. y.; Wang, R. t.; Wang, F.; Tong, S. f.; Jia, J. t.; Gao, Z. m.; Cai, Z. q., Experimental and numerical investigations of motion and mass transfer of single bubbles in a turbulent flow chamber. *J Taiwan Inst Chem Eng* **2022,** 136, 104435.
15. He, H.; Liu, Z.; Ji, J.; Li, S., Analysis of Interaction and Flow Pattern of Multiple Bubbles in Shear-Thinning Viscoelastic Fluids. *Energies* **2023,** 16, (14).
16. Ying, H.; Puzhen, G.; Chaoqun, W., Experimental and Numerical Investigation of Bubble–Bubble Interactions during the Process of Free Ascension. *Energies* **2019,** 12, (10).
17. Barreiro-Villaverde, D.; Gosset, A.; Mendez, M. A., On the dynamics of jet wiping: Numerical simulations and modal analysis. *Phys. Fluids* **2021,** 33, (6), 062114.
18. Chen, Y.; Luo, J.; Wu, F.; Zhang, Z.; Zhao, Z.; Zhang, L.; Luo, C.; Li, X., Multi-objective optimization on flow characteristics of pressure swirl nozzle: A LES-VOF simulation. *Int. J. Heat Mass Transf.* **2022,** 133, 105926.
19. Liu, Z. m.; Li, Z. m.; Liu, J. b.; Wu, J. c.; Yu, Y. s.; Ding, J. w., Numerical Study on Primary Breakup of Disturbed Liquid Jet Sprays Using a VOF Model and LES Method. *Processes* **2022,** 10, (6), 1148.
20. Saeedipour, M.; Schneiderbauer, S., Favre-filtered LES-VOF of two-phase flows with eddy viscosity-based subgrid closure models: An a-posteriori analysis. *Int. J. Multiphase Flow* **2021,** 144, 103780.
21. Zhang, J.; Liu, Y. f.; Gong, B.; Li, X.; Li, Y. x.; Wu, J. h., Dynamic Characteristic Analysis of a Single Droplet in a Liquid-Liquid Concave-Wall Jet. *Chemical Engineering & Technology* **2022,** 45, (5), 918-929.
22. Zhang, X. s.; Zhao, W. w.; Wan, D. c., A Hybrid Volume-of-Fluid/Euler-Lagrange Method for Vertical Plunging Jet Flows. *Int. J. Offshore Polar Eng.* **2022,** 32, (1), 31-38.
23. Ouyang, Y.; Zou, H. K.; Gao, X. Y.; Chu, G. W.; Xiang, Y.; Chen, J. F., Computational fluid dynamics modeling of viscous liquid flow characteristics and end effect in rotating packed bed. *Chem. Eng. Process.* **2018,** 123, 185-194.
24. Vivekanand, S. V. B.; Raju, V. R. K., Effect of wall contact angle and carrier phase velocity on the flow physics of gas-liquid Taylor flows inside microchannels. *Chem. Zvesti* **2018,** 73, (5), 1173-1188.

25. Daskiran, C.; Xue, X. z.; Cui, F. d.; Katz, J.; Boufadel, M. C., Large eddy simulation and experiment of shear breakup in liquid-liquid jet: Formation of ligaments and droplets. *Int. J. Heat Fluid Flow* **2021,** 89, 108810.
26. Charin, A. H. L. M.; Lage, P. L. C.; Silva, L. F. L. R.; Tuković, Ž.; Jasak, H., On the dynamic behavior of rising droplets. *Int. J. Multiphase Flow* **2019,** 110, 165-178.
27. Zhang, J.; Zhou, Y. y.; Gong, B.; Li, Y.; Liu, H. l.; Wu, J. h., Flow characteristics of three-dimensional concave-wall jet. *CIESC J.* **2019,** 70, (4), 1340-1348.
28. Zhang, J.; Li, X.; Gong, B.; Li, Y. x.; Wang, W.; Wang, S. c.; Wu, J. h., Numerical simulation and instability analysis of particles in liquid-solid concave-wall jet using DPM-RSM. *Asia-Pacific Journal of Chemical Engineering* **2022,** 17, (3), e2765.
29. O Ubbink, R. I. I., A Method for Capturing Sharp Fluid Interfaces on Arbitrary Meshes on Arbitrary Meshes. *J. Comput. Phys.* **1999,** 153, (1), 26-50.
30. Zhang, J.; Gao, Y. b.; Gong, B.; Li, Y. x.; Wu, J. h., Experimental investigation on single-droplet deformation and breakup in a concave-wall jet. *Chemical Engineering & Technology* **2020,** 44, (2), 238-247.
31. Constantinescu, G.; Miyawaki, S.; Rhoads, B.; Sukhodolov, A.; Kirkil, G., Structure of turbulent flow at a river confluence with momentum and velocity ratios close to 1: Insight provided by an eddy-resolving numerical simulation. *Water Resour. Res.* **2011,** 47, (5), W05507.
32. Liang, X.; Wang, X.; Lu, S.; Wang, K.; Luo, G., Pressure drop analysis for the droplet break-up flow in a locally constrictive microchannel. *Chem. Eng. Sci.* **2021,** 230, 116190.